Journal of Materials Chemistry B

ROYAL SOCIETY OF CHEMISTRY

PAPER

View Article Online
View Journal | View Issue

Cite this: J. Mater. Chem. B, 2025, 13, 1474

Lipid droplet specific BODIPY based rotors with viscosity sensitivity to distinguish normal and cancer cells: impact of molecular conformation†

Charutha Kalarikkal,[a] Anjali,‡[b] Sarbani Bhattacharjee,‡[b] Koyeli Mapa*[b] and Chinna Ayya Swamy P*[a]

Lipid droplets (LDs) are dynamic, multifunctional organelles critical for regulating energy balance, cell signaling, membrane formation, and trafficking. Recent studies have highlighted LDs as emerging cancer biomarkers, with cancer cells typically exhibiting a higher number and viscosity of LDs compared to normal cells. This discovery paves the way for developing molecular probes that can monitor intracellular viscosity changes within LDs, offering a powerful tool for early cancer diagnosis, recurrence monitoring, and therapeutic interventions. In this study, we designed and synthesized two series of donor–acceptor (D–A) conjugated BODIPY-cyanostilbene based fluorophores (**5a–c** and **6a–c**) by fine-tuning the cyanostilbene unit with three distinct substituents (OMe, H, Cl) and modulating the molecular conformation *via* rigidifying the indacene core. While the terminal substituents had a minimal effect on the optical properties, changes in molecular conformation significantly impacted the photophysical behavior of the fluorophores. Compounds **5a–c** function as molecular rotors, with the free rotation of the *meso*-biphenyl rings leading to non-radiative deactivation of the excited state, resulting in weak emission. Additionally, this structural feature makes them highly responsive to changes in viscosity. As the glycerol concentration increased from 0% to 99%, the fluorescence intensity of compounds **5a**, **5b**, and **5c** increased dramatically by 17-fold, 78-fold, and 43-fold, respectively. In contrast, compounds **6a–c**, with restricted phenyl ring rotation due to tetra-methyls on the indacene unit, showed only a modest 2–3-fold increment in fluorescence intensity under similar conditions. These fluorophores possess several key advantages, including high selectivity for LDs, good photostability, sensitivity to viscosity, and responsiveness to polarity and pH. Moreover, they effectively differentiate between normal and cancer cells, making them valuable tools for cancer diagnosis and potential therapeutic applications.

Received 26th October 2024,
Accepted 8th December 2024

DOI: 10.1039/d4tb02405b

rsc.li/materials-b

1. Introduction

Lipid droplets (LDs), once considered simple fat reserves within cells, are now recognized as dynamic organelles playing pivotal roles in maintaining energy homeostasis.[1] Structurally, LDs are composed of a core of neutral lipids like triglycerides and cholesterol esters, encased in a phospholipid monolayer embedded with specific proteins.[2,3] This configuration helps LDs to prevent lipotoxicity by regulating cellular stress responses and assist in lipid trafficking, protein storage, and degradation.[4–6] LDs also interact with other organelles including mitochondria, the endoplasmic reticulum, lysosomes, and peroxisomes, coordinating cellular metabolism.[6,7] A particularly significant aspect of LD biology is the impact of cellular viscosity on their functionality. Viscosity influences cellular processes like molecular diffusion, signal transduction, and enzymatic activities, which can regulate apoptosis, metabolism, and membrane formation.[8] Disruptions in LD function are linked to several diseases, including obesity, diabetes, non-alcoholic fatty liver disease, atherosclerosis, cardiovascular disease, and cancer.[3,9] Recent findings have uncovered a link between LDs and cancer, with malignant cells often displaying higher numbers, larger sizes, and greater motility of LDs compared to normal cells.[10] This relationship emphasizes the potential of LDs as biomarkers for cancer detection, treatment, and prognosis. Therefore, understanding their dynamics and cellular functions opens new avenues for

[a] Main group Organometallics Optoelectronic Materials and Catalysis lab, Department of Chemistry, National Institute of Technology, Calicut, 673601, India. E-mail: swamy@nitc.ac.in
[b] Protein Homeostasis Laboratory, Department of Life Sciences, School of Natural Sciences, Shiv Nadar Institution of Eminence, Delhi-NCR, Greater Noida, Gautam Buddha Nagar, Uttar Pradesh 201314, India

† Electronic supplementary information (ESI) available. See DOI: https://doi.org/10.1039/d4tb02405b

‡ Equal contribution.

therapeutic interventions, particularly in metabolic and cancer-related diseases.

Traditional techniques, including Raman microscopy, transmission light microscopy, electron microscopy, and mass spectrometry, have been crucial for visualizing LDs.[11] However, their practical applicability is limited by several factors, including intricate sample preparation, difficulty in real-time tracking of sub-cellular changes, low cell permeability, and the need for cell fixation.[11,12] Fluorescence imaging has revolutionized this field by offering non-invasive, real-time imaging of living cells including LDs, with high spatial and temporal resolution using specially designed fluorescent probes.[13–15] To date, many small molecular probes have been developed that target LDs including commercially used Nile Red and BODIPY 493/503.[16–19] However, these probes still face significant challenges, including non-specific binding to other intracellular components, poor photostability, and high background fluorescence. Additionally, the spectroscopic limitations reduce their effectiveness in multimodal imaging techniques.[20] As a result, the development of more efficient and selective probes remains essential to improve the accuracy of LD visualization and to better understand their dynamic behavior in live cells.

In the realm of small organic molecular probes, 4,4′-difluoro-4-bora-3*a*,4*a*-diaza-*s*-indacene also known as boron dipyrromethene (BODIPY) and their derivatives stand out due to the structural versatility, excellent photostability, high quantum yields, low cytotoxicity, high biocompatibility, and strong lipophilicity making them ideal for LD staining.[21,22] These properties have made them invaluable across diverse fields, including biological sensing, optoelectronics, and as photosensitizers.[23] A notable advancement in BODIPY research is the use of *meso*-substituted BODIPY derivatives as molecular rotors to study intracellular viscosity at the single-cell level. Kuimova *et al.* pioneered this approach in 2008 by modifying the *meso*-position of the BODIPY core to measure viscosity using fluorescence lifetime imaging microscopy (FLIM).[24] In low viscosity environments, these probes exhibit weak fluorescence due to non-radiative deactivation, while high viscosity restricts rotation, enhancing fluorescence.[25,26] Similarly, cyanostilbene-based organic fluorophores have gained significant attention due to their rigid and twisted structure, strong solid-state luminescence, and twisted intramolecular charge transfer (TICT) characteristics. They exhibit a wide range of applications including organic solar cells, organic light-emitting devices, liquid crystal displays, bioimaging, sensing, molecular switches and so on.[27] However, there is still scope for enhancement in the field of molecular rotors such as developing organelle-specific rotors to provide disease related insights, more photostable probes suited for multi modal imaging and super resolution microscopy, and minimal sensitivity to solvent polarity and temperature which are key attributes for achieving high spatial resolution and rapid data acquisition in live-cell imaging.

Our research centres on the design, synthesis, and characterization of a new class of donor–acceptor (D–A) conjugated BODIPY-cyanostilbene-based fluorophores (**5a–c** and **6a–c**), which specifically target LDs and distinguish normal cells from cancer cells by detecting intracellular viscosity variations. A standout feature of these fluorophores is their high selectivity towards viscosity, showing minimal interference from other environmental factors such as solvent polarity, pH changes, or the presence of competing species, making them highly suitable for the accurate tracking of dynamic physicochemical processes within LDs. We optimized their photophysical properties through two strategies: introducing different terminal groups (OMe, H, Cl) on the cyanostilbene moiety and incorporating four methyl groups to the BODIPY core to modify molecular conformation. Although modifications at the *meso*-position had minimal impact on optical properties, changes in conformation significantly affected the electronic interaction between the BODIPY and cyanostilbene units, thereby influencing their photophysical behavior. Compounds **5a–c** showed low fluorescence in low-viscosity environments due to free rotation causing non-radiative deactivation, but exhibited enhanced fluorescence in high-viscosity environments, making them highly sensitive molecular rotors. In contrast, **6a–c** adopted a rigid conformation due to steric effects of the methyl groups, exhibiting bright fluorescence even in low-viscosity environments but reduced sensitivity to viscosity changes. Our study shows that compounds **5a–c**, in particular, are well-suited for applications where sensitivity to viscosity is critical, such as the real-time imaging of intracellular environments or distinguishing between normal and cancerous cells. This research paves the way for the development of next-generation fluorophores with enhanced selectivity, photostability, and tunability, which could have broad implications in both bioimaging and therapeutic diagnostics.

2. Results and discussion

2.1 Synthesis and spectroscopic analysis

In the present work, we aimed to develop and synthesize two distinct series of D–A conjugated BODIPY-based fluorophores (**5a–c** and **6a–c**), carefully designed by fine-tuning the cyanostilbene derivatives and varying the molecular conformation to enhance their optical properties (Chart 1). The design strategy focused on two key aspects: (1) introducing three different terminal substituents (OMe, H, Cl) at the cyanostilbene core to modulate electronic effects, and (2) incorporating four methyl groups at the indacene unit of the BODIPY core to control the molecular conformation. The synthetic routes leading to the target molecules **5a–c** and **6a–c** are detailed in Scheme 1, and the full synthetic procedures are provided in the ESI.† To summarize, the synthetic strategy employed a stepwise approach, starting with the synthesis of intermediates, followed by cross-coupling reactions and achieved the desired products. The first step involved the Knoevenagel condensation reaction between 4-bromo benzaldehyde and the corresponding benzyl cyanides. This reaction proceeded efficiently, producing the desired intermediates **1a–c** in excellent yields. Next, the intermediates **1a–c** were subjected to palladium-catalyzed Suzuki–Miyaura

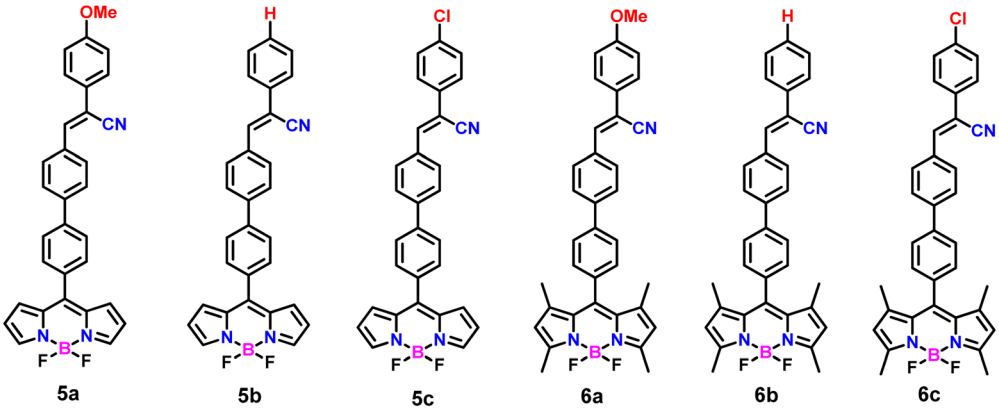

Chart 1 Chemical structures of compounds **5a–c** and **6a–c**.

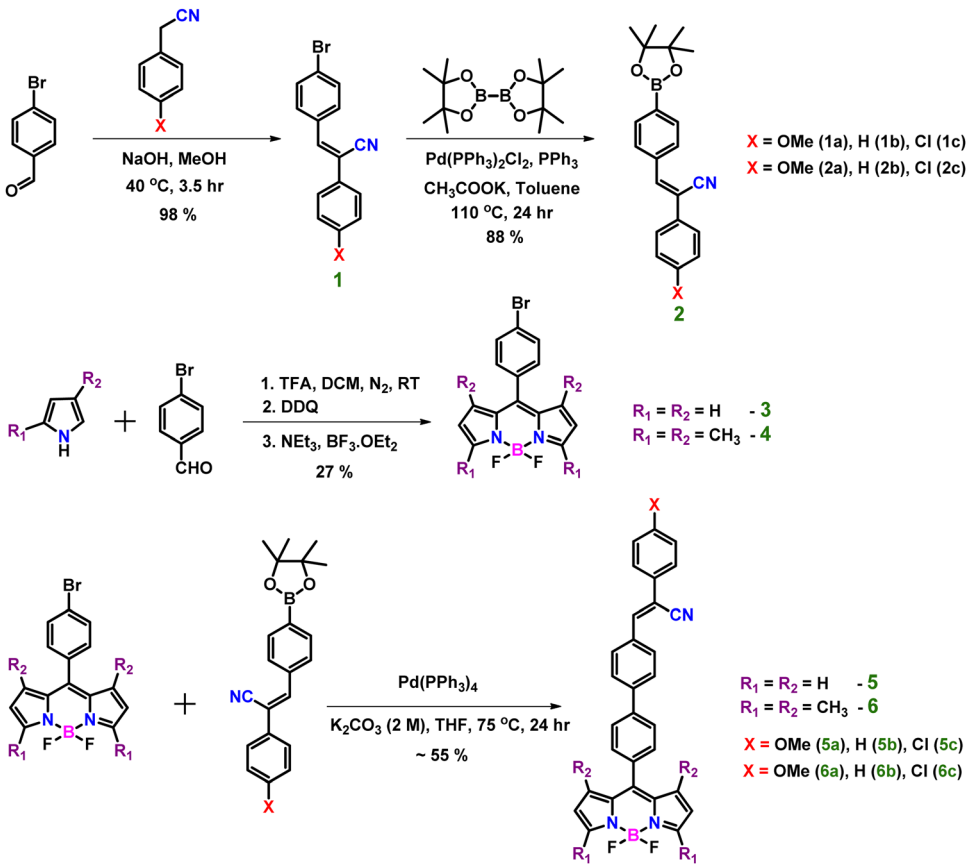

Scheme 1 Synthetic scheme adopted for the target molecules.

cross-coupling reaction yielding compounds **2a–c**. Furthermore, the synthesis of compounds **3** and **4**, which form the core BODIPY structures, were synthesized through a two-step process. First, a trifluoroacetic acid (TFA)-catalyzed condensation of 4-bromo benzaldehyde with the corresponding pyrroles was performed. This reaction produced the dipyrromethane intermediates, which were subjected to oxidation reaction by using DDQ (2,3-dichloro-5,6-dicyano-1,4-benzoquinone) to form the dipyrromethene scaffold. In the final step, the dipyrromethenes were complexed with $BF_3{\cdot}Et_2O$ in dichloromethane (CH_2Cl_2), resulting in the formation of the stable BODIPY cores (compounds **3** and **4**). In the final synthetic step, compounds **3** and **4** underwent palladium-catalyzed Suzuki–Miyaura cross-coupling reactions with the intermediates **2a–c**. This reaction allowed for the attachment of the cyanostilbene moiety to the BODIPY core, which leads to the formation of target molecules **5a–c** and **6a–c**. All newly synthesized compounds were thoroughly characterized using a range of advanced analytical techniques such as

^{1}H NMR, ^{13}C NMR, ^{11}B NMR, and ^{19}F NMR spectroscopy, as well as high-resolution mass spectrometry (HRMS) to confirm their structure and purity.

2.2 Photophysical properties

The preliminary photophysical properties of our target molecules (**5a–c** and **6a–c**) were investigated in dichloromethane (DCM) solvent, and the corresponding UV-vis absorption and fluorescence spectra are shown in Fig. 1 and Fig. S40 (ESI†). A comprehensive summary of the collected data is provided in Table 1. The UV-vis absorption spectra of the synthesized compounds fall within the range of 300–550 nm. For compound **5a**, three prominent absorption bands were observed as a strong absorption band around 500 nm, corresponding to the BODIPY $\pi \rightarrow \pi^*$ ($S_0 \rightarrow S_1$) transition, the cyanostilbene $\pi \rightarrow \pi^*$ transition ($\sim$360 nm), and a broad peak around $\sim$410–480 nm which might be due to the transitions resulting from the electronic interactions between the BODIPY core and the cyanostilbene unit. Compounds **5b** and **5c** displayed similar absorption patterns, with a peak around 500 nm, also characteristic of the BODIPY $\pi \rightarrow \pi^*$ transition and higher-energy transitions near 340 nm, corresponding to the cyanostilbene $\pi \rightarrow \pi^*$ transition, along with a shoulder peak around 385 nm that may be indicative of weak electronic communication between the BODIPY and cyanostilbene chromophores. Similarly, compounds **6a–c** displayed similar absorption profiles, featuring two absorption bands. The lower energy transition ($\sim$501 nm) originates from the $\pi \rightarrow \pi^*$ ($S_0 \rightarrow S_1$) transition of the BODIPY core, while the higher energy transition ($\sim$350 nm) is associated with the $\pi \rightarrow \pi^*$ transition of the cyanostilbene unit. Interestingly, the comparable absorption behavior across all synthesized compounds, regardless of the terminal substituents on the cyanostilbene unit, suggested only weak electronic coupling between the BODIPY core and cyanostilbene unit.[28,29] The absorption spectra of compounds **6a–c** appeared to be the sum of individual contributions from both chromophores, indicating minimal electronic conjugation between them.[30] To investigate the effect of terminal substituents on the cyanostilbene unit and their influence on the emission spectra, we conducted fluorescence studies in DCM using an excitation wavelength of 350 nm, specifically targeting the cyanostilbene moiety. This approach allowed us to directly assess how the different substituents modulate the photophysical behavior of the compounds. For example, for compounds **5a–c**, excitation at 350 nm led to a strong emission band between 520–525 nm, which corresponds to the $S_1 \rightarrow S_0$ transition of the BODIPY core. Additionally, a weak and broad emission band was observed in the 380–480 nm region, characteristic of the cyanostilbene moiety. This dual emission pattern indicates partial excitation energy transfer from the cyanostilbene donor to the BODIPY acceptor. Such energy transfer is dependent on several factors, including spectral overlap between the emission of the cyanostilbene donor and the absorption of the BODIPY acceptor, favorable orientation of the two chromophores, and their close proximity.[31,32] The weak residual cyanostilbene emission suggests that energy transfer in compounds **5a–c** is partial, likely due to the free rotation of the phenyl rings attached to the BODIPY core, which disrupts efficient energy transfer. In contrast, compounds **6a–c** exhibited a complete energy transfer from donor (cyanostilbene) to acceptor (BODIPY). Upon excitation at 350 nm, these compounds displayed a single, intense emission band around 515 nm, corresponding to the $S_1 \rightarrow S_0$ transition of the BODIPY core, with no observable emission from the cyanostilbene unit. This suggests that complete excitation energy transfer occurs from the cyanostilbene donor to the BODIPY acceptor in compounds **6a–c**. The higher efficiency of energy transfer in these compounds can be attributed to the restricted rotation of the phenyl rings, likely caused by the steric hindrance introduced by the methyl groups on the indacene unit.[31,32] This structural rigidity allows for better electronic coupling between the donor and acceptor, resulting in complete energy transfer. A slight bathochromic shift was noted in the emission spectra of compounds **5a–c** compared to compounds **6a–c**. This shift is attributed to the electronic communication between the BODIPY core and cyanostilbene units, which influence the emission wavelength. Furthermore, the fluorescence quantum yields of compounds **5a–c** were much lower than that of compounds

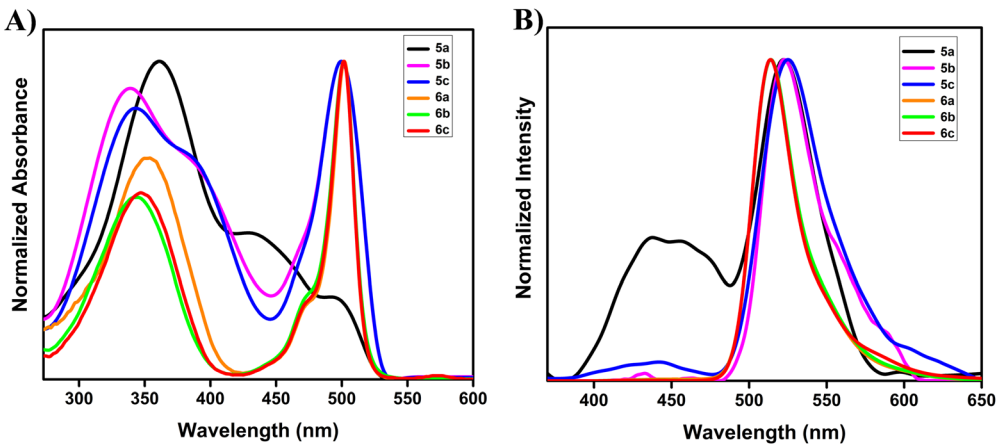

Fig. 1 (A) Normalized absorption (10 μM) and (B) normalized emission spectra of compounds **5a–c** and **6a–c** in DCM (2 μM, λ_{ex} = 350 nm).

Table 1 Photophysical data of the compounds

Compounds	λ_{abs} (nm)/ε ($\times 10^4$)	λ_{em} (nm)	$\Phi_f{}^a$
5a	361 (2.9), 428 (1.3), 499 (0.8)	438, 522	06
5b	339 (3.1), 500 (3.3)	524	07
5c	343 (3.0), 500 (3.5)	525	10
6a	352 (2.9), 500 (3.2)	515	50
6b	344 (2.5), 501 (4.3)	514	50
6c	347 (1.6), 501 (2.6)	515	54

[a] Quantum yields are calculated using quinine sulfate (0.1 M in H_2SO_4, Φ_F = 57.7%) solution as a reference and using the following formula $\phi = \phi_F \times I/I_R \times A_R/A \times \eta^2/\eta_R{}^2$ where ϕ = quantum yield, I = integral area of the emission peak, A = absorbance at λ_{ex}, and η = refractive index of the solvent.

6a–c. This reduced intensity is likely a consequence of the free rotation of the biphenyl rings in compounds **5a–c**, leading to non-radiative deactivation of the excited state, as described in Table 1.[22,28] Moreover, we can conclude that varying the terminal substitutions on the cyanostilbene unit had minimal impact on the optical properties of our target molecules.

2.3 Spectral response to viscosity

After thoroughly analyzing the fundamental optical properties of our target molecules, we shifted our focus to examining their molecular rotor characteristics by precisely studying the relationship between fluorescence intensity and viscosity. To achieve this, we controlled the viscosity of the environment by varying the ratios of DMSO and glycerol in a miscible system, creating a viscosity range from 2 cP (DMSO) to 878.32 cP (glycerol). This setup allowed us to assess how changes in viscosity impacted the photophysical behavior of the target compounds. Our results, depicted in Fig. 2, and Fig. S41, S42 (ESI†), demonstrate that compound **5b** exhibited a very weak fluorescence emission at 525 nm when excited at 350 nm in pure DMSO (2 cP), a low-viscosity solvent. This weak emission is primarily attributed to the intramolecular free rotation of the *meso* bi-phenyl rings in **5b**, which facilitates non-radiative deactivation of the excited state. As the viscosity increased with the addition of glycerol, the photophysical behavior of **5b** changed dramatically. With increasing glycerol concentration (0% to 99%), the maximum fluorescence intensity of **5b** increased by a remarkable 78-fold. This sharp increase in fluorescence intensity can be attributed to the restriction of intramolecular rotation in the higher-viscous environment. When the intramolecular motion is hindered, the molecule is forced to undergo radiative decay rather than non-radiative processes, leading to a significant enhancement in fluorescence emission.[33,34] The behavior of compounds **5a** and **5c** followed a similar trend to **5b**, with fluorescence intensity enhancements of 17-fold and 43-fold, respectively. This suggests that for all the compounds in the **5a–c** series, the intramolecular free rotation of the *meso* bi-phenyl rings is the dominant factor influencing fluorescence intensity in low-viscous environments, and restricting this rotation *via* increasing viscosity leads to a notable fluorescence enhancement. Furthermore, the incorporation of an electron-donating methoxy

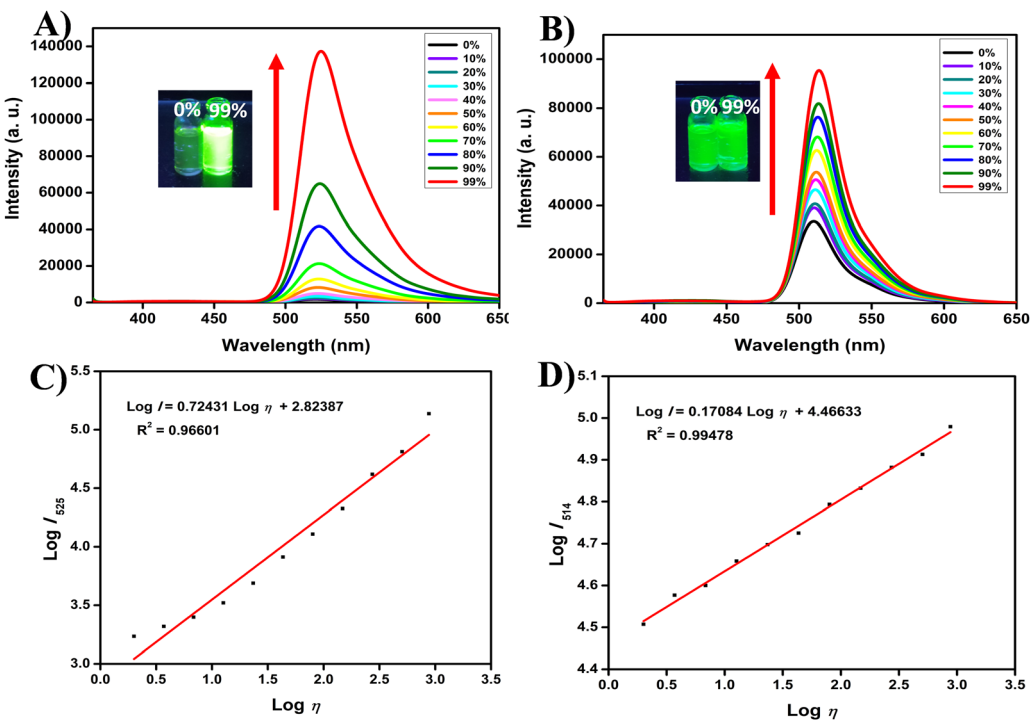

Fig. 2 Emission spectra of compounds (A) **5b** (10 μM, λ_{ex} = 350 nm), and (B) **6b** (1 μM, λ_{ex} = 350 nm), in DMSO–glycerol mixtures with increasing concentration of glycerol from 0% to 99%. Inset photos taken under a UV 365 nm lamp are displayed on the top of the spectra. Linear relationship between log I (fluorescence intensity) and log η (viscosity) of compounds **5b** (C), and **6b** (D).

(OMe) group at the cyanostilbene unit in **5a** promotes free rotation of the rotatable single bonds, causing non-radiative deactivation of the excited state. This is evidenced by the notably lower quantum yield of **5a** compared to **5b** and **5c**, along with the different electronic distributions observed in DFT studies (discussed in detail in Section 2.5 DFT Studies). Additionally, the free rotation of the methoxy group might have increased the energy barrier, even in highly viscous environments, resulting in reduced sensitivity to viscosity. In the case of **5b** and **5c**, DFT studies indicate similar electronic distributions; however, **5b** exhibits a slightly lower quantum yield than **5c**, suggesting faster non-radiative decay. The terminal substitution (–Cl) in **5c** likely increases the energy barrier slightly compared to **5b**, resulting in lower viscosity sensitivity for **5c**. These results are consistent with previous reports,[35] which emphasize the critical role of the energy barrier in determining viscosity sensitivity. For **5b**, the faster non-radiative decay and lower energy barrier could explain its enhanced sensitivity to viscosity relative to the other compounds. In contrast to the **5a–c** series, **6a–c** displayed only modest increment in the fluorescence intensity (2 to 3-fold) as the viscosity was increased. This limited response is attributed to the structural rigidity introduced by the four methyl groups on the indacene unit of the **6a–c** series. The presence of these methyl groups significantly reduces the free rotation of the *meso* bi-phenyl rings, even in low-viscous environments like DMSO. As a result, compounds **6a–c** already exhibit relatively strong fluorescence emission in low-viscosity conditions, and their fluorescence increases only marginally with higher viscosity. Furthermore, the orthogonal orientation effectively decouples the two chromophores resulting in a minimal effect of terminal substitutions on their optical properties, particularly viscosity sensitivity. In addition to the qualitative observations, we also analyzed the relationship between fluorescence intensity and viscosity quantitatively. Across all the target molecules, we found an excellent linear correlation between the logarithm of fluorescence intensity ($\log I$) and the logarithm of viscosity ($\log \eta$) within the viscosity range of 2 cP to 878.32 cP, as illustrated by the Förster–Hoffmann equation:[36,37]

$$\log I = C + x \log \eta \quad (1)$$

In this equation, I represent the fluorescence intensity, C is a constant, x corresponds to the sensitivity of the compound to viscosity, and η denotes the viscosity of the solution. This linear relationship confirms that the fluorescence response of the target molecules is highly dependent on the surrounding viscosity, and the slope (x) provides a direct measure of each compound's sensitivity to viscosity changes. The results of our study suggest that the **5a–c** series, with their sensitivity to viscosity-driven changes in fluorescence intensity, are particularly well-suited for applications as molecular rotors. These compounds, especially **5b**, show a robust and significant response to varying viscosity, with a clear restriction of intramolecular motion resulting in dramatic fluorescence enhancements. Such behavior is ideal for probing microenvironmental viscosity, particularly in dynamic systems such as LDs or other cellular compartments where viscosity may fluctuate over time.

2.4 Selectivity and competitive studies

To further investigate the influence of solvent polarity on both the ground and excited states of our target molecules, we conducted a series of absorption and emission studies across solvents with varying dielectric constants. The results, outlined in Table S1 and Fig. S43 (ESI†), reveal that the absorption spectra of the target molecules (**5a–c** and **6a–c**) remained consistent with all solvents, implying that the ground-state electronic structure is not affected by the solvent environment.[30] This indicates that the electronic transitions responsible for absorption are not significantly altered by the polarity of the medium. On the other hand, the fluorescence spectra showed only very slight changes in intensity with the solvent polarity, which strongly suggested the minimal effect of the solvent environment on the excited-state properties of the compounds (Fig. 3A, B and Fig. S44, ESI†). However, a stark contrast emerged when we examined the fluorescence behavior of the compounds in viscous media, which we have discussed detailed in the previous section.

Next, to evaluate the selectivity of these compounds towards other competing factors, we conducted fluorescence studies in the presence of various ions (Zn^{2+}, Fe^{3+}, Cu^{2+}, Na^{+}, K^{+}, Ca^{2+}, CO_3^{2-}, HCO_3^{-}, and NO_2^{-}), amino acids (Ser, Asn, Thr, and Tyr), reactive oxygen species (ClO^{-} and H_2O_2) and reactive sulphur species (GSH, Cys, and Hcy), which are common in biological systems (Fig. 3C, D and Fig. S45, ESI†). The results showed no significant change in fluorescence intensity in response to the presence of these ions, confirming that the fluorescence response of the compounds is highly specific to viscosity variations. This specificity is significant for biological applications, as it ensures that the compounds can reliably detect changes in viscosity without interference from fluctuations in ion concentration. We also investigated the effect of pH on the fluorescence behavior of the compounds, given that pH levels vary widely within different cellular compartments and between healthy and diseased tissues. For this purpose, we tested compounds **5b** and **6b** in two viscosity environments: DMSO (low-viscosity) and a 1 : 1 mixture of glycerol/DMSO (high-viscosity) (Fig. 3E, F and Fig. S46, ESI†). The results revealed that the fluorescence intensity of all compounds remained constant across a wide pH range, confirming that pH changes have minimal impact on their optical properties. However, a significant increase in fluorescence intensity was observed when the viscosity increased, independent of pH.[36] Overall, our findings demonstrate that the target molecules exhibit robust photophysical properties with a high degree of sensitivity to viscosity changes while maintaining stability against solvent polarity, pH variations, and interference from other biological species. These characteristics make them ideal candidates for probing the microenvironment of LDs and other intracellular structures where viscosity plays a key role in cellular function and disease progression. The excellent selectivity and responsiveness of these compounds lay a strong foundation for their further development as fluorescent probes in bioimaging and diagnostic applications.

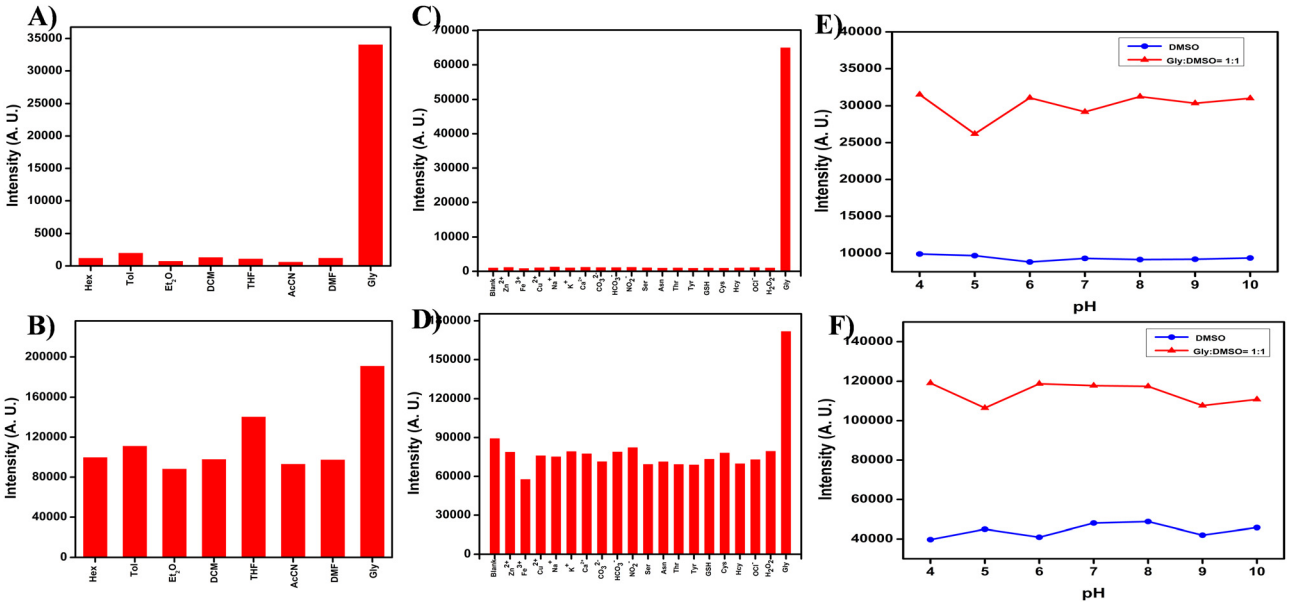

Fig. 3 Fluorescence responses of compounds (A) **5b** (2 μM) and (B) **6b** (2 μM), in solvents of different polarity (hexane, toluene, diethyl ether, DCM, THF, AcCN, DMF, glycerol). Fluorescence responses of compounds (C) **5b** (2 μM) and (D) **6b** (2 μM), in DMSO with various analytes (100 μM) (Blank), $Zn(OAc)_2$, $FeCl_3$, $Cu(OAc)_2$, NaCl, KCl, $CaCl_2$, K_2CO_3, $NaHCO_3$, $NaNO_2$, Ser, Asn, Thr, Tyr, GSH, Cys, Hcy, OCl^-, H_2O_2, and Glycerol. Fluorescence responses of compounds (E) **5b** (2 μM) and (F) **6b** (2 μM), at different pH values and viscous solutions (DMSO and DMSO : glycerol= 1 : 1) (λ_{ex} = 350 nm).

2.5 DFT studies

To further understand the structural and electronic characteristics of the target molecules, density functional theory (DFT) calculations were carried out for compounds **5a–c** and **6a–c**. These calculations were aimed at exploring how molecular conformation and terminal substituents affect their electronic properties. The computations were conducted using Gaussian 09W, with the B3LYP/6-31G(d,p) level of theory in the gas phase, without enforcing symmetry constraints.[38] One key focus of the study was to evaluate the dihedral angles between the *meso*-phenyl ring and the BODIPY core, as these angles significantly influence the degree of conjugation between the two chromophores (Fig. S47, ESI†). For compounds **5a–c**, the dihedral angle was calculated to be approximately 53°, suggesting that the *meso*-phenyl ring and the BODIPY core are not completely planar but still allow for partial electronic interaction. This partial conjugation promotes a moderate degree of electronic communication between the two chromophores, influencing the optical behavior of the molecules, particularly with respect to energy transfer and fluorescence properties. In contrast, compounds **6a–c** exhibited a much larger dihedral angle, around 90°, indicating that the *meso*-phenyl ring is orthogonal to the BODIPY core. This orthogonal orientation, caused by steric hindrance from the methyl groups on the indacene unit, decouples the two chromophores, preventing significant electronic interaction.[31] The DFT calculations also provided insights into the electronic distribution within the molecules (Fig. 4 and Table S2, Fig. S48, ESI†). In compounds **5b** and **5c**, the highest occupied molecular orbitals (HOMOs) and lowest unoccupied molecular orbitals (LUMOs) are more confined to the BODIPY core, while the HOMO−1 and LUMO+1 are situated on the cyanostilbene units. Specifically, in compound **5a**, the presence of an electron-donating OMe group shifts the localization of the HOMO and LUMO+1 to the cyanostilbene unit, while the HOMO−1 and LUMO remain on the BODIPY core. The non-orthogonal orientation of the *meso* phenyl ring in compounds **5a–c**, leads to moderate mixing of the molecular orbitals (MOs) between the two chromophores, particularly the LUMO and LUMO+1 orbitals, while the HOMO−1 and HOMO orbitals remain unaffected. Conversely, for compounds **6a–c**, the orbital distribution shows a distinct separation between the chromophores. In compounds **6a** and **6b**, the electronic distribution is confined to the indacene unit for HOMO and LUMO orbitals, while the HOMO−1 and LUMO+1 orbitals are localized on the cyanostilbene units. In the case of compound **6c**, the HOMO and LUMO+1 orbitals are concentrated on the indacene unit, while the HOMO−1 and LUMO are localized on the cyanostilbene derivative. This complete localization of the electronic distribution to each chromophore implies that the absorption spectra of **6a–c** represent a simple summation of the individual chromophore contributions, with minimal inter-chromophore interaction. Additionally, the introduction of various terminal substituents on the cyanostilbene unit-OMe (electron-donating), H (neutral), and Cl (electron-withdrawing) has very little effect on the absorption spectra of compounds **6a–c**. This is due to the orthogonal orientation of the *meso*-phenyl ring, which inhibits significant electronic communication between the chromophores. In contrast, compounds **5a–c**, with their non-orthogonal *meso*-phenyl rings, allow for moderate orbital overlap between the cyanostilbene and BODIPY units. This partial orbital mixing enhances electronic communication in compounds **5a–c**, leading

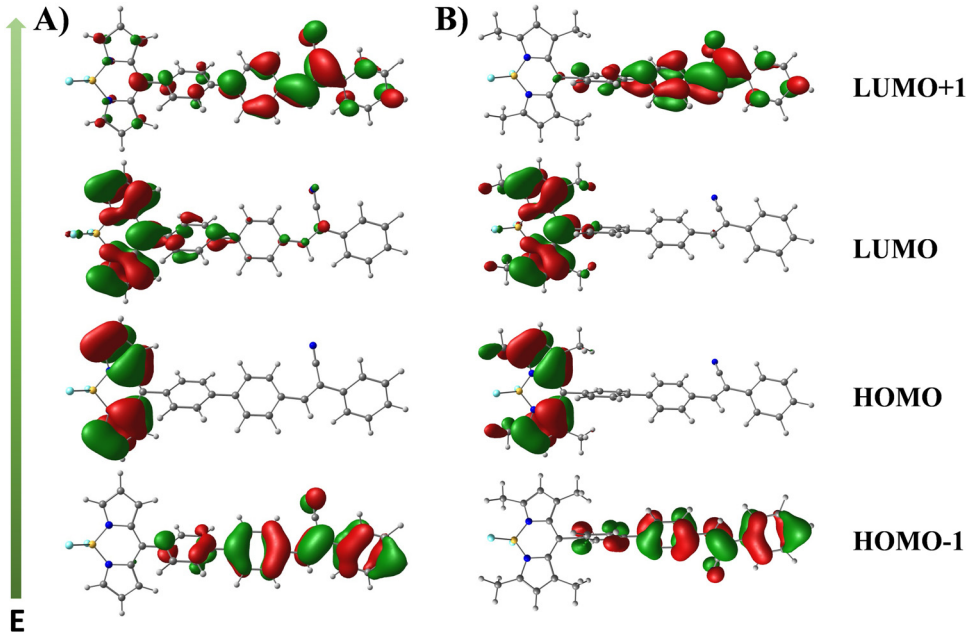

Fig. 4 Important frontier molecular orbitals (MOs) of compounds **5b** (A), and **6b** (B). Calculations were based on the optimized ground state geometry at the B3LYP/6-31G(d,p) level with Gaussian 09.

to more pronounced optical effects and sensitivity to environmental changes. However, the emission spectra may still vary based on energy transfer efficiency between the cyanostilbene and BODIPY units. This structural and orbital distinction underlies the different properties observed between the two series of compounds.

To further understand the photophysical behavior of the target compounds, time-dependent density functional theory (TD-DFT) calculations were performed to examine their UV-vis absorption properties in the gas phase. These calculations were based on the ground-state optimized geometries and employed the Franck–Condon principle to simulate vertical excitations. The predicted electronic transitions, their oscillator strengths, and the molecular orbitals involved are detailed in both Fig. S49 and Table S3 (ESI†). For compounds **5b** (λ_{max} calc. = 354 nm, λ_{max} exp. = 339 nm), **5c** (λ_{max} calc. = 360 nm, λ_{max} exp. = 345 nm), **6a** (λ_{max} calc. = 360 nm, λ_{max} exp. = 350 nm), and **6b** (λ_{max} calc. = 383 nm, λ_{max} exp. = 343 nm), the predominant transition originates from HOMO−1 to LUMO+1, corresponding to the $\pi \rightarrow \pi^*$ transition of the cyanostilbene unit. In contrast, for compound **5a** (λ_{max} calc. = 377 nm, λ_{max} exp. = 360 nm), the major excitation involves a transition from HOMO to LUMO+1, whereas compound **6c** (λ_{max} calc. = 367 nm, λ_{max} exp. = 348 nm) shows a similar transition, originating from HOMO−1 to LUMO, involving the cyanostilbene unit. The lower energy transition (λ_{max} exp. = 500 nm) for compounds **5b** (λ_{max} calc.= 415 nm), **5c** (λ_{max} calc. = 419 nm), **6a** (λ_{max} calc. = 409 nm), and **6b** (λ_{max} calc. = 409 nm), is from HOMO to LUMO, corresponding to the $\pi \rightarrow \pi^*$ ($S_0 \rightarrow S_1$) transition of the BODIPY core. For compound **5a** (λ_{max} calc. = 412 nm), the lower energy transition occurs between HOMO−1 to LUMO, while in compound **6c** (λ_{max} calc. = 410 nm), it involves HOMO to LUMO+1 transitions. Additionally, the broad peak in compound **5a** may stem from overlapping electronic transitions between the BODIPY core and cyanostilbene unit, reflecting their partial conjugation. Overall, these calculated results align well with the experimental UV-vis absorption data, validating the presence of distinct electronic transitions in both chromophore systems.

2.6 Lipid droplet specificity

To further assess the potential of our target compounds for bioimaging applications, we conducted an in-depth evaluation of their performance in live-cell imaging. First, the cytotoxicity of the compounds was tested on HeLa cells using the 3-[4,5-dimethylthiazol-2-yl]-2,5-diphenyltetrazolium bromide (MTT) assay, which measures cell viability following compound exposure. Cells were treated with increasing concentrations of the compounds for 24 hours. As illustrated in Fig. S50 (ESI†), the compounds displayed low cytotoxicity, with cell viability remaining above 90% at concentrations as high as 1 μM. Although a decrease in cell viability was noted at higher concentrations, it is important to emphasize that the concentrations necessary for effective cellular imaging are much lower, approximately 500 nM, thereby reducing any concerns about potential toxicity during imaging studies. Next, we examined the cellular localization of the compounds using confocal fluorescence microscopy. Upon treatment with the compounds, HeLa cells exhibited distinct fluorescence localized in small, punctate structures within the cytoplasm. These bright fluorescent spots suggested a potential accumulation in organelles, and their distribution and appearance led us to hypothesize that the compounds were likely localizing in LDs, as seen with similar fluorescent probes.[24,39] To confirm this hypothesis, co-localization studies were performed using Nile Red, a well-known

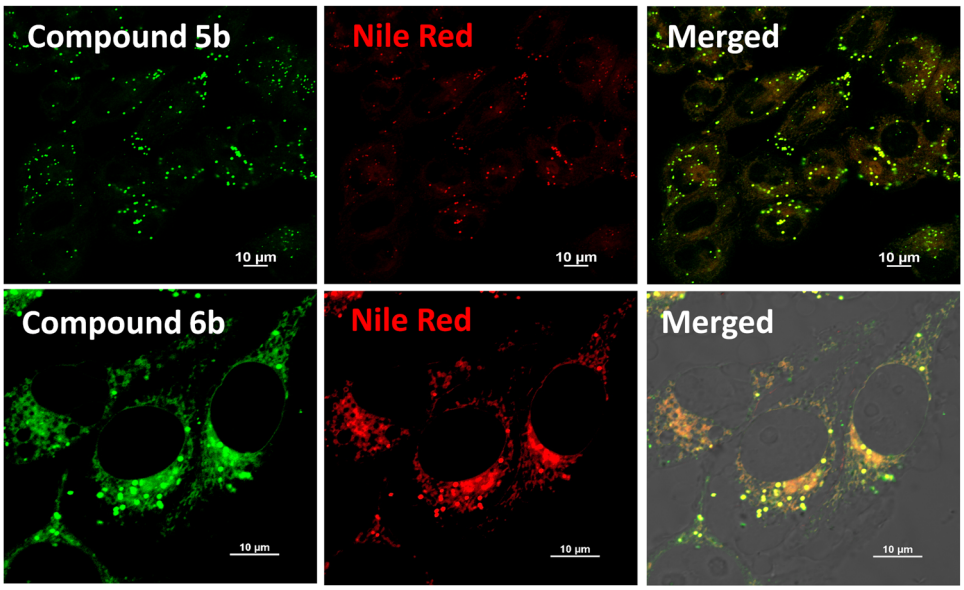

Fig. 5 Confocal fluorescence microscopy images of intracellular co-localization in HeLa cells. Cells were incubated with compounds **5b** and **6b** (500 nM) (left), commercially available lipid droplet staining Nile Red (middle), and the merged images (right).

LD marker, as shown in Fig. 5 and Fig. S51 (ESI†). The green fluorescence of the compounds and the red fluorescence of Nile Red showed complete overlap, confirming that the compounds selectively target LDs within the cells and the Pearson's correlation coefficient was determined to be 0.83 for compound **5b** and 0.85 for compound **6b** (Fig. S51, ESI†). The LD specificity of our target fluorophores is likely due to their highly conjugated aromatic structure, which imparts lipophilic properties and exhibits a strong tendency to accumulate within the hydrophobic core of LDs.[26] In addition to the Nile Red experiments, further co-localization studies were carried out using other organelle-specific dyes, including Mito-Tracker (for mitochondria), Lyso-Tracker (for lysosomes), and Hoechst (for nuclei), as illustrated in Fig. S52 (ESI†). No significant overlap was observed between these markers and the fluorescence of the compounds, further reinforcing their selective localization to LDs. Interestingly, we observed a marked difference in fluorescence intensity between the two series of compounds. Compounds **6a–c** consistently exhibited stronger fluorescence signals compared to **5a–c**. This difference may be attributed to the molecular rotor behavior of the **5a–c** series, which is more prone to intramolecular motions that can quench fluorescence, whereas the **6a–c** series has a more rigid molecular structure, preventing such quenching and resulting in higher fluorescence intensity. This enhanced fluorescence makes the **6a–c** series particularly promising for high-sensitivity imaging. Furthermore, we have also evaluated the photostability of our target fluorophores. As shown in Fig. S53 and S54 (ESI†), the fluorescence intensity remained nearly unchanged over 50 minutes, indicating that the probes exhibit good photostability over an extended period. Taken together, these findings highlight the strong potential of both series of compounds for selective LD imaging in living cells, with excellent biocompatibility and minimal cytotoxicity, and good photostability. The superior brightness of the **6a–c** series suggests that they could be especially useful in applications requiring high-contrast imaging, while the unique properties of the **5a–c** series may offer additional advantages in dynamic studies of LD behavior. These results pave the way for further exploration of these compounds in advanced bioimaging techniques.

2.7 Discriminating normal cells and cancer cells

Cancer remains one of the most critical global health challenges, with its high mortality rate continuing to drive the search for more effective diagnostic and therapeutic approaches. Among the emerging biomarkers, LDs have gained attention due to their increased number and altered properties in cancer cells.[10,40] LDs play a crucial role in vital processes such as energy metabolism, oxidative stress regulation, and autophagy all of which are closely tied to cancer progression.[6] Notably, cancer cells tend to have more LDs with higher viscosity compared to their normal cells.[10,41] Leveraging this information, we conducted an experiment to test whether our compounds could differentiate cancer cells from normal cells by targeting these unique LD characteristics. In this study, HEK293T cells were selected as the model for non-cancerous cells, while HeLa cells served as the cancer cell model. Both cell types were exposed to identical experimental conditions, followed by fluorescence imaging. As shown in Fig. 6 and Fig. S55 and S56 (ESI†), the fluorescence images revealed a clear distinction between the two cell types. HeLa cells showed a marked increase in the number of LDs, as well as significantly stronger fluorescence intensity compared to HEK293T cells, which exhibited only faint fluorescence when treated with the same compounds. This clear contrast in fluorescence response between cancer and normal cells is likely due to the dual effect of a higher quantity of LDs and increased viscosity in cancer cells. Quantitative analysis of the fluorescence intensity

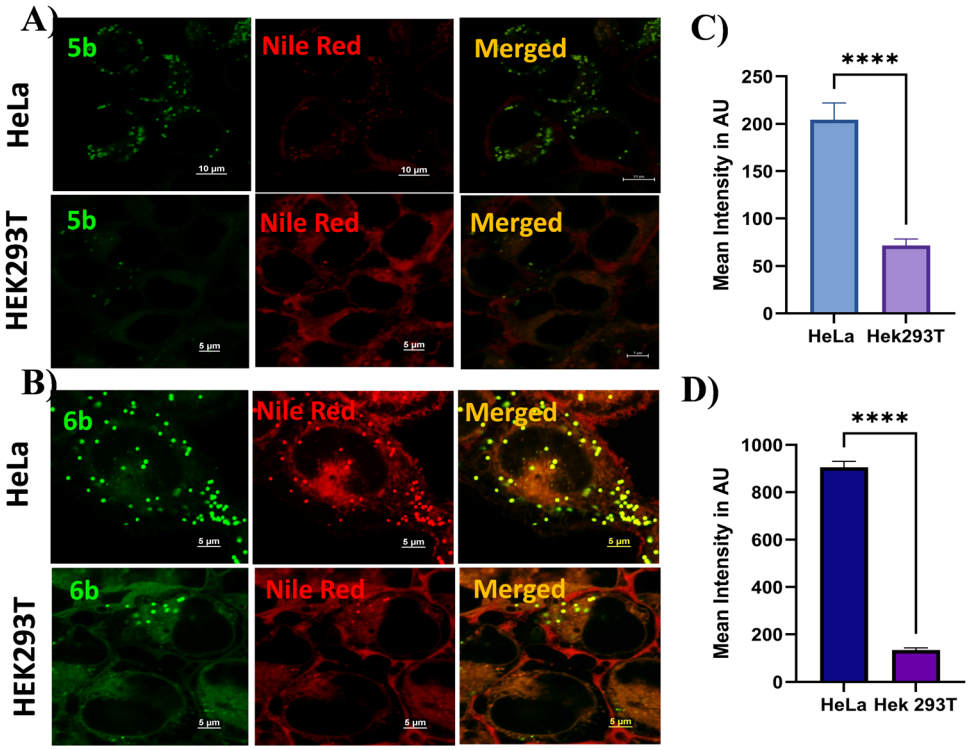

Fig. 6 Confocal fluorescence microscopy images of different living cells incubated with compounds **5b** (A) and **6b** (B) (500 nM) (left), commercially available lipid droplet staining Nile Red (middle), and the merged images (right) including normal cells (HEK293T) and cancer cells (HeLa). Quantitative changes in the fluorescence intensities of compounds **5b** (C), and **6b** (D) in cancer cells and normal cells.

confirmed that compounds **5a**, **5b**, and **5c** produced 8.7-fold, 2.8-fold, and 7.4-fold enhanced fluorescence in HeLa cells compared to HEK293T cells, respectively. Similarly, compounds **6a**, **6b**, and **6c** demonstrated 12.7-fold, 6.8-fold, and 3.3-fold enhanced fluorescence in HeLa cells than in HEK293T cells. These findings suggest that the unique characteristics of LDs in cancer cells can be exploited for selective targeting. By utilizing the differences in LD number and viscosity, our compounds demonstrate a strong potential for distinguishing cancer cells from normal cells. This approach could provide a valuable tool for cancer detection and may also be applicable in developing new strategies for targeted cancer therapies.

3. Conclusions

In this study, we introduced two novel series of D–A conjugated BODIPY-cyanostilbene fluorophores (**5a–c** and **6a–c**), designed by varying the terminal groups on the cyanostilbene unit (OMe, H, Cl) and manipulating molecular conformation through the addition of methyl groups on the indacene core. Our findings revealed that altering the *meso*-position of the BODIPY core had minimal influence on the optical properties of the fluorophores, while controlling the conformation of the molecules played a crucial role in fine-tuning the electronic communication between the BODIPY and cyanostilbene chromophores, significantly impacting their photophysical behavior. Compounds **5a–c** demonstrated weak fluorescence in low-viscosity media due to free rotation around the *meso*-phenyl rings, which enabled non-radiative decay of the excited state. However, in high-viscosity environments like glycerol, this rotation was restricted, resulting in a remarkable increase in emission. Specifically, the fluorescence intensity of compounds **5a**, **5b**, and **5c** increased by 17-fold, 78-fold, and 43-fold, respectively, with increasing glycerol concentration (0% to 99%). In contrast, compounds **6a–c**, with methyl groups on the indacene unit that limit free rotation, displayed strong fluorescence even in low-viscosity media, and only a modest 2–3-fold increase was observed in high-viscosity conditions. These experimental results were further correlated by density functional theory (DFT) and time-dependent DFT (TD-DFT) calculations, which highlighted the role of molecular conformation in influencing the optical properties. Beyond their sensitivity to viscosity, the fluorophores exhibited excellent selectivity to polarity and pH, along with minimal interference from other biological molecules, making them versatile probes for biological systems. A key highlight of these fluorophores is their selective localization in LDs, which are known to be involved in various metabolic processes and are often upregulated in cancer cells. The compounds displayed a clear ability to differentiate cancer cells from normal cells, leveraging the increased number and viscosity of LDs in cancer cells. This property suggests that these fluorophores could serve as useful tools for cancer diagnosis, enabling early detection through the monitoring of LD behavior. Additionally, their strong response to environmental changes and good photostability makes them valuable candidates for a

wide range of biological applications, particularly in imaging and diagnostic fields.

Data availability

The data supporting this article have been included as part of the ESI.†

Conflicts of interest

There are no conflicts to declare.

Acknowledgements

C. A. S. P. sincerely acknowledges the Science and Engineering Research Board (SERB) for the EEQ grant (EEQ/2021/000180). C. K. gratefully thanks the Department of Science and Technology, New Delhi, for awarding the DST-Inspire Fellowship (IF210349). C. K. and C. A. S. P. also thank NIT Calicut for the NMR (CMC), HRMS (DST-FIST) and HPC (CCMS) facility. K. M. acknowledges the funding support from the Science and Engineering Research Board (SERB), Government of India, for Core Research Grant (SERB/CRG/2022/006517) and SNIoE core funding. A. N. and S. B. acknowledge the SNIoE PhD fellowship. A. N., S. B. and K. M. acknowledge the SNU DST-FIST grant [SR/FST/LS-1/2017/59(c)] for the confocal microscopy facility. We thank Rajan Singh for his help at the confocal microscopy facility at SNIoE.

References

1 R. V. J. Farese and T. C. Walther, Lipid droplets finally get a little respect, *Cell*, 2009, **139**, 855–860.
2 J. A. Olzmann and P. Carvalho, Dynamics and functions of lipid droplets, *Nat. Rev. Mol. Cell Biol.*, 2019, **20**, 137–155.
3 A. Zadoorian, X. Du and H. Yang, Lipid droplet biogenesis and functions in health and disease, *Nat. Rev. Endocrinol.*, 2023, **19**, 443–459.
4 F. Geltinger, L. Schartel, M. Wiederstein, J. Tevini, E. Aigner, T. K. Felder and M. Rinnerthaler, Friend or foe: lipid droplets as organelles for protein and lipid storage in cellular stress response, aging and disease, *Molecules*, 2020, **25**, 5053–5083.
5 E. Jarc and T. Petan, Lipid droplets and the management of cellular stress, *Yale J. Biol. Med.*, 2019, **92**, 435–452.
6 (*a*) M. Gao, X. Huang, B.-L. Song and H. Yang, The biogenesis of lipid droplets: lipids take center stage, *Prog. Lipid Res.*, 2019, **75**, 100989–100999; (*b*) M. F. Renne and H. Hariri, Lipid droplet-organelle contact sites as hubs for fatty acid metabolism, trafficking, and metabolic channeling, front, *Cell Dev. Biol.*, 2021, **9**, 726261–726271; (*c*) Y. Jin, Y. Tan, J. Wu and Z. Ren, Lipid droplets: a cellular organelle vital in cancer cells, *Cell Death Discovery*, 2023, **9**, 254–262; (*d*) J. Z. Hsia, D. Liu, L. Haynes, R. Cruz-Cosme and Q. Tang, Lipid droplets: formation, degradation, and their role in cellular responses to flavivirus infections, *Microorganisms*, 2024, **12**, 647–670.
7 Y.-X. Zhou, S.-Y. Wu, X. Zhang and F.-G. Wu, Lipid droplet-targeting optical biosensors: design strategies and applications, *Anal. Chem.*, 2024, **175**, 117703–117729.
8 (*a*) D. Su, C. L. Teoh, L. Wang, X. Liu and Y.-T. Chang, Motion-induced change in emission (MICE) for developing fluorescent probes, *Chem. Soc. Rev.*, 2017, **46**, 4833–4844; (*b*) J. Yin, L. Huang, L. Wu, J. Li, T. D. James and W. Lin, Small molecule based fluorescent chemosensors for imaging the microenvironment within specific cellular regions, *Chem. Soc. Rev.*, 2021, **50**, 12098–12150.
9 B. C. Farmer, A. E. Walsh, J. C. Kluemper and L. A. Johnson, Lipid droplets in neurodegenerative disorders, *Front. Neurosci.*, 2020, **14**, 742–754.
10 A. L. S. Cruz, E. A. Barreto, N. P. B. Fazolini, J. P. B. Viola and P. T. Bozza, Lipid droplets: platforms with multiple functions in cancer hallmarks, *Cell Death Dis.*, 2020, **11**, 105–120.
11 T. K. Fam, A. S. Klymchenko and M. Collot, Recent advances in fluorescent probes for lipid droplets, *Materials*, 2018, **11**, 1768–1786.
12 H. Kobayashi, M. Ogawa, R. Alford, P. L. Choyke and Y. Urano, New strategies for fluorescent probe design in medical diagnostic imaging, *Chem. Rev.*, 2010, **110**, 2620–2640.
13 H. Zhu, J. Fan, J. Du and X. Peng, Fluorescent probes for sensing and imaging within specific cellular organelles, *Acc. Chem. Res.*, 2016, **49**, 2115–2126.
14 H. Tian, A. C. Sedwick, H.-H. Han, S. Sen, G.-R. Chen, Y. Zang, J. L. Sessler, T. D. James, J. Li and X.-P. He, Fluorescent probes for the imaging of lipid droplets in live cells, *Coord. Chem. Rev.*, 2021, **427**, 213577–213590.
15 Y. Zhao, W. Shi, X. Li and H. Ma, Recent advances in fluorescent probes for lipid droplets, *Chem. Commun.*, 2022, **58**, 1495–1509.
16 L. Wang, X. Chen, X. Ran, H. Tang and D. Cao, Recent advance of lipid droplets fluorescence imaging with aggregation-induced emission luminogens (AIEgens), *Dyes Pigm.*, 2022, **203**, 110332–110345.
17 P. Greenspan, E. P. Mayer and S. D. Fowler, Nile red: a selective fluorescent stain for intracellular lipid droplets, *J. Cell Biol.*, 1985, **100**, 965–973.
18 B. Qiu and M. C. Simon, BODIPY 493/503 staining of neutral lipid droplets for microscopy and quantification by flow cytometry, *Bio-Protoc.*, 2016, **6**, e1912.
19 E. E. Spangenburg, S. J. P. Pratt, L. M. Wohlers and R. M. Lovering, Use of BODIPY (493/503) to visualize intramuscular lipid droplets in skeletal muscle, *J. Biomed. Biotechnol.*, 2011, 598358.
20 M. Collot, T. K. Fam, P. Ashokkumar, O. Faklaris, T. Galli, L. Danglot and A. S. Klymchenko, Ultrabright and fluorogenic probes for multicolor imaging and tracking of lipid droplets in cells and tissues, *J. Am. Chem. Soc.*, 2018, **140**, 5401–5411.
21 (*a*) J. Karolin, L. B.-A. Johansson, L. Strandberg and T. Ny, Fluorescence and absorption spectroscopic properties of

dipyrromethene boron difluoride (BODIPY) derivatives in liquids, lipid membranes, and proteins, *J. Am. Chem. Soc.*, 1994, **116**, 7801–7806; (*b*) R. Ziessel, G. Ulrich and A. Harriman, The chemistry of Bodipy: a new *el dorado* for fluorescence tools, *New J. Chem.*, 2007, **31**, 496–501; (*c*) L. D. Lavis and R. T. Raines, Bright ideas for chemical biology, *ACS Chem. Biol.*, 2008, **3**, 142–155; (*d*) N. Boens, V. Leen and W. Dehaen, Fluorescent indicators based on BODIPY, *Chem. Soc. Rev.*, 2012, **41**, 1130–1172; (*e*) H. Lu, J. Mack, Y. Yang and Z. Shen, Structural modification strategies for the rational design of red/NIR region BODIPYs, *Chem. Soc. Rev.*, 2014, **43**, 4778–4823.

22 (*a*) A. Loudet and K. Burgess, BODIPY dyes and their derivatives; syntheses and spectroscopic properties, *Chem. Rev.*, 2007, **107**, 4891–4932; (*b*) G. Ulrich, R. Ziessel and A. Harriman, The chemistry of fluorescent Bodipy dyes: versatility unsurpassed, *Angew. Chem., Int. Ed.*, 2008, **47**, 1184–1201.

23 (*a*) P. Kaur and K. Singh, Recent advances in the application of BODIPY in bioimaging and chemosensing, *J. Mater. Chem. C*, 2019, **7**, 11361–11405; (*b*) M. Poddar and R. Misra, Recent advances of BODIPY based derivatives for optoelectronic applications, *Coord. Chem. Rev.*, 2020, **421**, 213462–213683; (*c*) B. M. Squeo, L. Ganzer, T. Virgili and M. Pasini, *Molecules*, 2021, **26**, 153–182; (*d*) F.-Z. Li, Z. Wu, C. Lin, Q. Wang and G.-C. Kuang, *Results Chem.*, 2022, **4**, 100384–100398; (*e*) I. S. Yadav and R. Misra, Design, synthesis and functionalization of BODIPY dyes: applications in dye-sensitized solar cells (DSSCs) and photodynamic therapy (PDT), *J. Mater. Chem. C*, 2023, **11**, 8688–8723; (*f*) D. Pinjari, Y. Patil and P. Misra, Near-infrared absorbing aza-BODIPY dyes for optoelectronic applications, *Chem. – Asian J.*, 2024, **19**, e202400167.

24 M. K. Kuimova, G. Yahioglu, J. A. Levitt and K. Suhling, Molecular rotor measures viscosity of live cells via fluorescence lifetime imaging, *J. Am. Chem. Soc.*, 2008, **130**, 6672–6673.

25 B. M. Uzhinov, V. L. Ivanov and M. Y. Melnikov, Molecular rotors as luminescence sensors of local viscosity and viscous flow in solutions and organized systems, *Russ. Chem. Rev.*, 2011, **80**, 1179–1190.

26 (*a*) K. Li, Y. Wang, Y. Li, W. Shi and J. Yan, Development of BODIPY-based fluorescent probes for imaging Aβ aggregates and lipid droplet viscosity, *Talanta*, 2024, **227**, 126362–126371; (*b*) G. Li, J. Li, Y. Otsuka, S. Zhang, M. Takahashi and K. Yamada, A BODIPY-based fluorogenic probe for specific imaging of lipid droplets, *Materials*, 2020, **13**, 677–686; (*c*) R. Žvirblis, K. Maleckaitė, J. Dodonova-Vaitkūnienė, D. Jurgutis, R. Žilėnaitė, V. Karabanovas, S. Tumkevičius and A. Vyšniauskas, A red-emitting thiophene-modified BODIPY probe for fluorescence lifetime-based polarity imaging of lipid droplets in living cells, *J. Mater. Chem. B*, 2023, **11**, 3919–3928; (*d*) M. Olšinová, P. Jurkiewicz, M. Pozník, R. Šachl, T. Prausová, M. Hof, V. Kozmík, F. Teplý, J. Svoboda and M. Cebecauer, Di- and tri-oxalkyl derivatives of a boron dipyrromethene (BODIPY) rotor dye in lipid bilayers, *Phys. Chem. Chem. Phys.*, 2014, **16**, 10688–10697; (*e*) J. Zhu, N. K. Tan, K. Kikuchi, A. Kaur and E. J. New, BODIPY-based fluorescent indicators for lipid droplets, *Anal. Sens.*, 2024, **4**, e202300049; (*f*) J. E. Chambers, M. Kubánková, R. G. Huber, I. López-Duarte, E. Avezov, P. J. Bond, S. J. Marciniak and M. K. Kuimova, An optical technique for mapping microviscosity dynamics in cellular organelles, *ACS Nano*, 2018, **12**, 4398–4407.

27 (*a*) L. Zhu and Y. Zhao, Cyanostilbene-based intelligent organic optoelectronic materials, *J. Mater. Chem. C*, 2013, **1**, 1059–1065; (*b*) B. Kim, H. R. Yeom, W.-Y. Choi, J. Y. Kim and C. Yang, Synthesis and characterization of a bis-methanofullerene-4-nitro-α-cyanostilbene dyad as a potential acceptor for high-performance polymer solar cells, *Tetrahedron*, 2012, **68**, 6696–6700; (*c*) P. Mahalingavelar and S. Kanvah, α-cyanostilbene: a multifunctional spectral engineering motif, *Phys. Chem. Chem. Phys.*, 2022, **24**, 23049–23075; (*d*) A. Gao, Q. Wang, H. Wu, J.-W. Zhao and X. Cao, Research progress on AIE cyanostilbene-based self-assembly gels: design, regulation and applications, *Coord. Chem. Rev.*, 2022, **471**, 214753–214775; (*e*) B.-K. An, J. Gierschner and S. Y. Park, π-conjugated cyanostilbene derivatives: a unique self-assembly motif for molecular nanostructures with enhanced emission and transport, *Acc. Chem. Res.*, 2012, **45**, 544–554; (*f*) S. Sasaki, G. P. C. Drummen and G.-I. Konishi, Recent advances in twisted intramolecular charge transfer (TICT) fluorescence and related phenomena in materials chemistry, *J. Mater. Chem. C*, 2016, **4**, 2731–2743; (*g*) M. Martínez-Abadía, R. Giménez and M. B. Ros, Self-assembled α-cyanostilbenes for advanced functional materials, *Adv. Mater.*, 2018, **30**, 1704161–1704199; (*h*) A. Afrin and P. C. A. Swamy, Symphony of light: AIE and MFC in carbazole-based cyanostilbenes, *J. Mater. Chem. C*, 2024, **12**, 1923–1944; (*i*) A. Afrin and P. C. A. Swamy, Tailoring emission color shifts in mechanofluorochromic-active AIE systems of carbazole-based d–π–a conjugates: impact of π spacer unit variants, *J. Org. Chem.*, 2024, **89**, 7946–7961; (*j*) A. Afrin and P. C. A. Swamy, Aggregation induced emission and reversible mechanofluorochromism active carbazole-anthracene conjugated cyanostilbenes with different terminal substitutions, *New J. Chem.*, 2023, **47**, 18919–18932.

28 T. Gayathri, A. K. Barui, S. Prashanthi, C. R. Patra and S. P. Singh, *meso*-Substituted BODIPY fluorescent probes for cellular bio-imaging and anticancer activity, *RSC Adv.*, 2014, **4**, 47409–47413.

29 R. P. Nandi, P. C. A. Swamy, P. Dhanalakshmi, S. K. Behera and P. Thilagar, Effect of the molecular conformation on excitation energy transferrin conformationally constrained boryl-BODIPY dyads, *Inorg. Chem.*, 2021, **60**, 5452–5462.

30 P. C. A. Swamy, S. Mukherjee and P. Thilagar, Multichannel-emissive V-shaped boryl-BODIPY dyads: synthesis, structure, and remarkably diverse response toward fluoride, *Inorg. Chem.*, 2014, **53**, 4813–4823.

31 P. C. A. Swamy, S. Mukherjee and P. Thilagar, Dual emissive borane-BODIPY dyads: molecular conformation control over electronic properties and fluorescence response towards fluoride ions, *Chem. Commun.*, 2013, **49**, 993–995.

32 J. R. Lakowicz, *Principles of fluorescence spectroscopy*, Springer, Singapore, 2006.
33 Y. Zhang, Z. Li, W. Hu and Z. Liu, A mitochondrial-targeting near-infrared fluorescent probe for visualizing and monitoring viscosity in live cells and tissues, *Anal. Chem.*, 2019, **91**, 10302–10309.
34 L. Zhang, G. Li, H. Zheng and W. Lin, A mitochondria-targeted fluorescent probe with viscosity sensitivity to distinguish normal and cancer cells, *New J. Chem.*, 2024, **48**, 4565–4569.
35 (*a*) X. Liu, W. Chi, Q. Qiao, S. V. Kokate, E. P. Cabrera, Z. Xu, X. Liu and Y.-T. Chang, Molecular mechanism of viscosity sensitivity in BODIPY rotors and application to motion-based fluorescent sensors, *ACS Sens.*, 2020, **5**, 731–739; (*b*) S. Toliautas, J. Dodonova, A. Žvirblis, I. Čiplys, A. Polita, A. Devižis, S. Tumkevičius, J. Šulskus and A. Vyšniauskas, Enhancing the viscosity-sensitive range of a BODIPY molecular rotor by two orders of magnitude, *Chem. – Eur. J.*, 2019, **25**, 10342–10349.
36 Y. Wu, W. Shu, C. Zeng, B. Guo, J. Shi, J. Jing and X. Zhang, A mitochondria targetable and viscosity sensitive fluorescent probe and its applications for distinguishing cancerous cells, *Dyes Pigm.*, 2019, **168**, 134–139.
37 M. Liu, J. Weng, S. Huang, W. Yin, H. Zhang, Y. Jiang, L. Yang and H. Sun, Water-soluble fluorescent probes for differentiating cancer cells and normal cells by tracking lysosomal viscosity, *Chem. Commun.*, 2023, **59**, 3570–3573.
38 N. Gupta, S. I. Reja, V. Bhalla, M. Gupta, G. Kaur and M. Kumar, A bodipy based fluorescent probe for evaluating and identifying cancer, normal and apoptotic C6 cells on the basis of changes in intracellular viscosity, *J. Mater. Chem. B*, 2016, **4**, 1968–1977.
39 (*a*) D. Jurgutis, G. Jarockyte, V. Poderys, J. Dodonova-Vaitkuniene, S. Tumkevicius, A. Vysniauskas, R. Rotomskis and V. Karabanovas, Exploring BODIPY-based sensor for imaging of intracellular microviscosity in human breast cancer cells, *Int. J. Mol. Sci.*, 2022, **23**, 5687–5703; (*b*) C. Caltagirone, M. Arca, A. M. Falchi, V. Lippolis, V. Meli, M. Monduzzi, T. Nylander, A. Rosa, J. Schmidt, Y. Talmon and S. Murgia, Solvatochromic fluorescent BODIPY derivatives as imaging agent in camptothecin loaded hexasomes for possible theranostic applications, *RSC Adv.*, 2015, **5**, 23443–23449.
40 D. Delmas, A. K. Cotte, J.-L. Connat, F. Hermetet, F. Bouyer and V. Aires, Emergence of lipid droplets in the mechanisms of carcinogenesis and therapeutic responses, *Cancers*, 2023, **15**, 4100–4116.
41 R. Munir, J. Lisec, J. V. Swinnen and N. Zaidi, Lipid metabolism in cancer cells under metabolic stress, *Br. J. Cancer*, 2019, **120**, 1090–1098.

